LUND UNIVERSITY

Reconstruction of Equivalent currents Using the Scalar Surface Integral Representation

Persson, Kristin; Gustafsson, Mats

2005

[Link to publication](#)

Reconstruction of equivalent currents using the scalar surface integral representation

Kristin Persson and Mats Gustafsson

Kristin Persson and Mats Gustafsson

Department of Electrical and Information Technology
Electromagnetic Theory
Lund University
P.O. Box 118
SE-221 00 Lund
Sweden

Abstract

Knowledge of the current distribution on a radome can be used to improve radome design, detect manufacturing errors, and to verify numerical simulations. In this paper, the transformation from near-field data to its equivalent current distribution on a surface of arbitrary material, *i.e.*, the radome, is analyzed. The transformation is based on the scalar surface integral representation that relates the equivalent currents to the near-field data. The presence of axial symmetry enables usage of the fast Fourier transform (FFT) to reduce the computational complexity. Furthermore, the problem is regularized using the singular value decomposition (SVD). Both synthetic and measured data are used to verify the method. The quantity of data is large since the height of the radome corresponds to $29 - 43$ wavelengths in the frequency interval $8.0 - 12.0$ GHz. It is shown that the method gives an accurate description of the field radiated from an antenna, on a surface enclosing it. Moreover, disturbances introduced by copper plates attached to the radome surface, not localized in the measured near field, are focused and detectable in the equivalent currents. The method also enables us to determine the phase shift of the field due to the passage of the radome, *cf.*, the insertion phase delay.

1 Introduction

This paper provides a wrap-up and a final report of the reconstruction of equivalent currents in the scalar approximation. The theoretical derivation is a summary of the work [11]. The new aspect in this report is mainly the analysis of the measured near-field data, especially the investigation of the phase information. Different ways of visualizing the results are also discussed and presented.

1.1 Ranges of application

There are several applications of a near field to equivalent currents transformation. For example, in the radome industry it is important to have accurate models of the field radiated from the antenna placed inside the radome. It is hard to measure this field directly since the radome often is located very close to the antenna and at these distances, there is a substantial interaction between the antenna and the measuring probe [6, 13, 19]. It is also important to have a powerful tool to determine the insertion phase delay (IPD), also known as the electrical thickness of the radome. The IPD is often one of the specified qualities given to characterize a radome. One way to measure the IPD is to place two horn antennas in such a way that the incident angle on the radome coincide with the Brewster angle, which is the angle where the transmitted field has its highest value [12]. To get the IPD, the phase of the transmitted field is subtracted from the phase of the measured field with no radome between the horn antennas. This process is very time consuming since it has to be repeated several times to cover the whole radome surface. Using the scalar surface integral equation, the phase shift due to the propagation through the radome is determined.

Another field of application is in the manufacturing of radiating bodies, *i.e.*, antenna arrays *etc.*, when the radiation pattern from the body does not exhibit the expected form. By determination of the equivalent currents on the radiating body, the malfunctioning areas or components can be found.

1.2 History

A common method, transforming near field to equivalent currents and vice versa, is to use modal-expansions of the electric field [6]. This is a very efficient method for radiating bodies with certain geometrical symmetries, *i.e.*, planar, cylindrical, and spherical. Having a planar aperture, the plane wave spectrum of the field is utilized in the back transformation [3, 5]. The fact that the expression of the far field originating from a planar surface is equal to the Fourier transform of the radiating field on the aperture has been investigated in [10, 13]. The paper [10] also illustrates that defects, *i.e.*, patches of Eccosorb, can be detected on the aperture. If the radiating body is of cylindrical or spherical geometry, the radial solutions contain cylindrical and spherical Bessel functions, while the angular solutions are described by trigonometric functions and the associated Legendre functions [6, 17]. For general geometrical symmetries, where modal-expansions do not exist, the modal-expansion is less applicable.

Moreover, different combinations of the electric- and magnetic-field integral equations (EFIE and MFIE) derived from the Maxwell equations, have been used to back propagate fields towards their sources, *i.e.*, a linear inverse source problem is solved. By this method it is possible to handle a wider class of geometries [13]. In [18] the dual-surface, magnetic and electric-field integral equations are investigated. The fields are transformed back to a cubic perfect electric conductor by solving the dual-surface magnetic-field integral equation using the conjugate gradient method. Other work using the integral equations is reported in [14], where the near field is measured on a arbitrary surface and later inverted to a planar, perfectly conducting surface by using a singular value decomposition (SVD) for regularization.

1.3 The scalar surface integral representation

In this paper, the approach is to investigate a scalar surface integral representation that does not require the aperture to be a perfect electric or magnetic conductor. The representation provides a relation relating the unknown electric and magnetic equivalent currents on a surface to the measured electric field. An additional relation is given by the fact that the equivalent currents are constructed such that the integral is zero inside the volume, on which surface the currents exist, *i.e.*, the extinction theorem [16].

The integral relations are discretized into matrix linear equations. The matrix equations include an azimuthal convolution which is solved with a fast Fourier transform (FFT) in the angular coordinate. The fast Fourier transform brings down the complexity of the problem, *i.e.*, the original surface-to-surface linear map is decomposed into a set of line-to-line linear maps. A singular value decomposition (SVD)
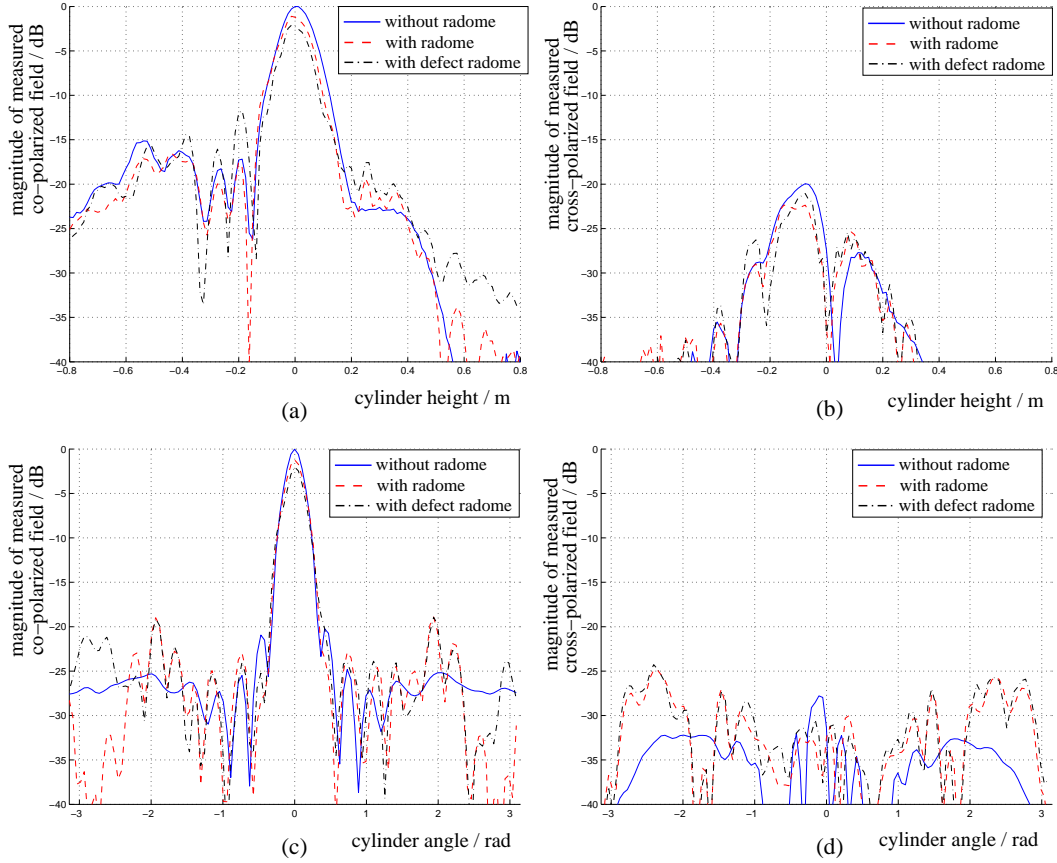
Figure 1: The measured co- and cross-polarized electric field on the measurement cylinder at 8.0 GHz. In (a) and (b) the angle is fixed at $\varphi = 0$, and the fields are normalized by the maximum value when no radome is present in (a). In (c) and (d) the height is fixed at $z = 0$, and the fields are normalized to the maximum value when no radome is present in (c).

is used to invert each of these linear maps. As most inverse problems it is ill-posed, *i.e.*, small errors in the near-field data can produce large errors in the equivalent currents. Thus, the problem needs to be regularized by suppression of small singular values when inverted.

1.4 Results

In this paper, the measured electric field is presumed to be scalar, *i.e.*, the scalar surface integral representation is utilized. The assumption is acceptable since the used near-field data, supplied by SAAB Bofors Dynamics and Applied Composites AB, Sweden, clearly have one dominating component in the main lobe, see Figure 1. The measured data is given for three different antenna and radome configurations, *viz.*, antenna, antenna together with radome, and antenna together with defect
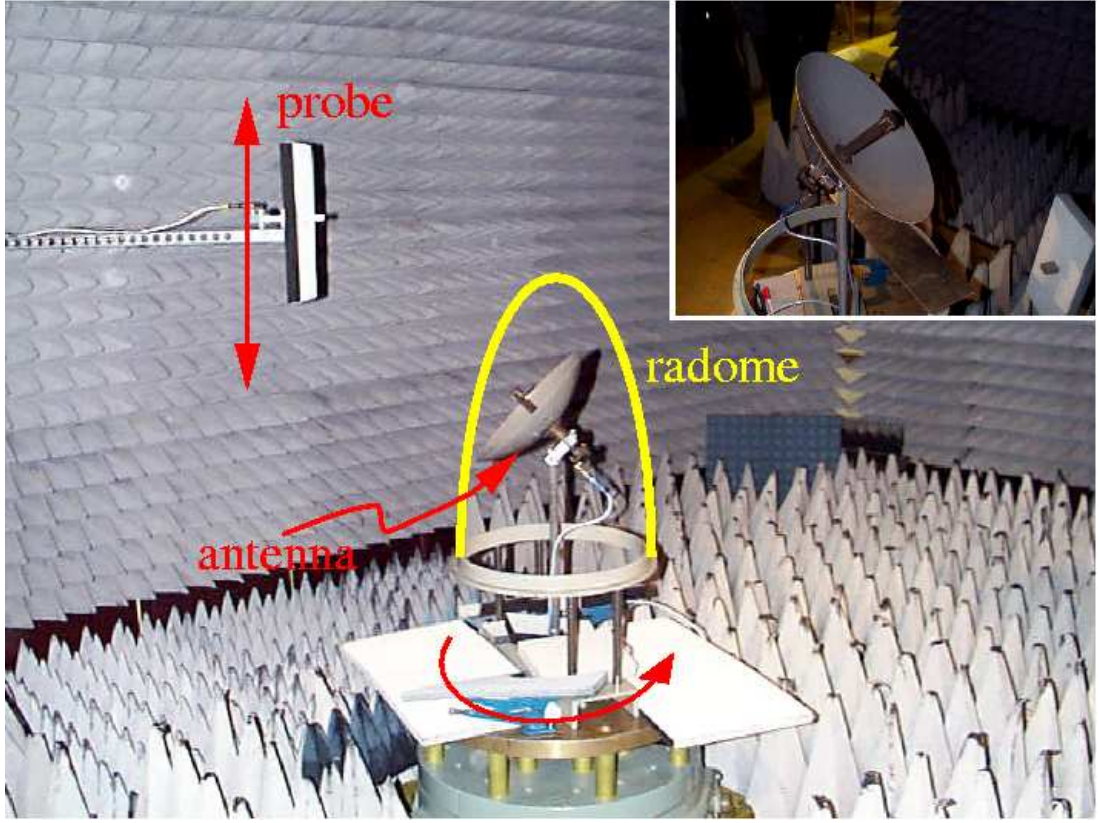
Figure 2: Photo of the cylindrical near-field range at SAAB Bofors Dynamics, Sweden. The antenna under test is rotated and the probe is moved in the vertical direction. A close up of the reflector antenna is shown in the upper right corner.

radome. The measurement set-up is shown in Figure 2. The height of the radome corresponds to $29 - 43$ wavelengths in the frequency interval $8.0 - 12.0\,\mathrm{GHz}$.

As a start, synthetic data is used to verify the method. Verification is also performed by a comparison between the measured far field and the far field calculated from the equivalent currents on the radome. The calculated far field agrees well with the measured far field. Moreover, when the radome is introduced, the field is scattered and flash lobes arise. The equivalent currents on the radome, due to these effects are identified and the flash lobes are accurately detected.

Manufacturing errors, not localized in the measured near-field data, can be focused and detected in the equivalent currents on the radome surface. In this paper, it is shown that the field scattered by copper plates attached on the radome, is focused back towards the original position of the copper plates. The length of the side of the square copper plates is $6\,\mathrm{cm}$, *i.e.*, $1.6 - 2.4$ wavelengths corresponding to the frequency span $8.0 - 12.0\,\mathrm{GHz}$.

1.5   Outline

In Section 2, the experimental set-up is described and the measured near-field data is presented. The scalar surface integral representation is introduced and adapted to the specific problem in Section 3. Section 4 contains the implementation process of the scalar surface integral representation. Results, using synthetic near-field data, and the error of the method are presented. The results, when using the experimental near-field data, are shown and examined in Section 5. To give the reader a understanding of the information that can be extracted from the resulting data, Section 6 gives examples of ways to visualize the results. The paper ends with the achieved conclusions in Section 7.

2   Near-field measurements

The near-field data, used in this paper, was supplied by SAAB Bofors Dynamics and Applied Composites AB, Sweden. The set-up with relevant dimensions indicated is shown in Figures 2 and 3a. Three different measurements were performed; data measured without the radome, data measured with the radome, and data measured with the defect radome. The defect radome has two copper plates attached to its surface.

A reflector antenna, fed by a symmetrically located wave-guide, generates the near-field, see Figure 2. The diameter of the antenna is $0.32\,\text{m}$ and its focal distance is $0.1\,\text{m}$. The main lobe of the antenna is vertically polarized relative to the horizontal plane. The standing wave ratio (SWR) is approximately 1.4 in the frequency range $8.2 - 9.5\,\text{GHz}$. The antenna is poorly adapted for other frequencies. A $10\,\text{dB}$ reflection attenuator is connected to the antenna.

The height of the radome surface is modeled by

$$\rho(z) = \begin{cases} 0.213\,\text{m} & -0.728\,\text{m} \le z \le -0.663\,\text{m} \\ -(bz' + d) + \sqrt{(bz' + d)^2 - a(z')^2 - 2cz' - e} & -0.663\,\text{m} < z \le 0.342\,\text{m} \end{cases}$$
(2.1)

where $z' = z + 0.728\,\text{m}$ and the constants are $a = 0.122$, $b = 0.048$, $c = -0.018\,\text{m}$, $d = 0.148\,\text{m}$, and $e = -0.108\,\text{m}^2$, respectively. The material of the radome has a relative permittivity of 4.32 and its loss tangent is 0.0144. The thickness of the wall of the radome varies between $7.6 - 8.2\,\text{mm}$. The near-field measurement probe consists of a wave-guide for which no compensation is made in the final data. The cylindrical surface, where the electric field is measured, is located in the near-field zone [2].

The amplitude and phase of the electric field are measured in the frequency interval $8.0 - 12.0\,\text{GHz}$ on a cylindrical surface by moving the probe in the z-direction and rotating the antenna under test, see Figure 2. With this measurement set-up, the fields on the top and the bottom of the cylindrical surface could not be collected. It would have been preferable to measure the fields on an infinite cylinder. However, the size of the cylinder is chosen such that the turntable below the radome does not have
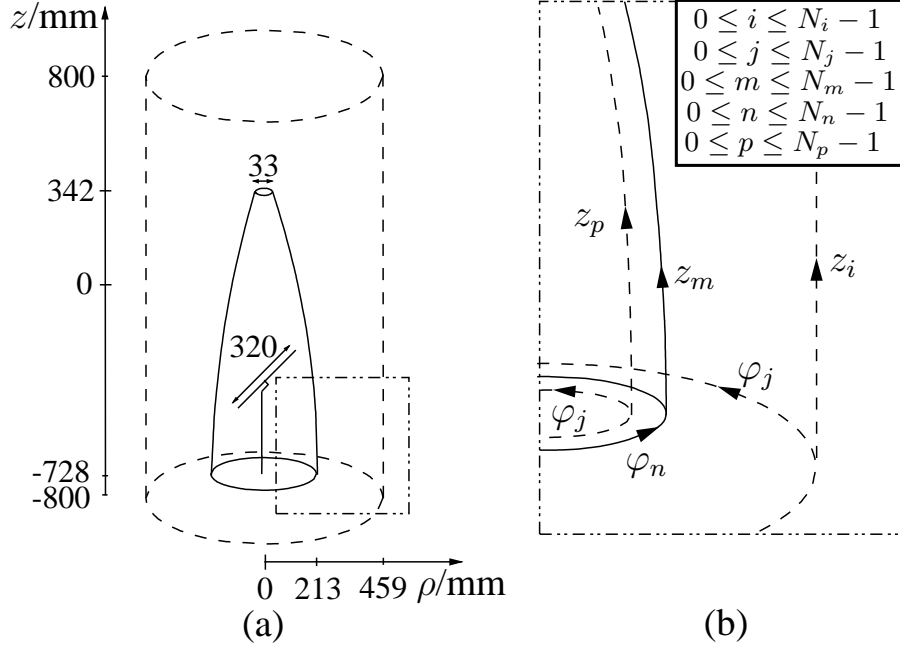
Figure 3: (a) The dimensions of the reflector antenna, the radome, and the cylinder where the electric near field is measured. (b) A close-up showing the inner fictitious surface and the discretized geometric variables.

a major influence of the measurements and such that the fields above $z = 800\,\text{mm}$ are negligible, *cf.*, Figures 1 and 3a. In the azimuth angle, 120 points are measured between $-180°$ and $180°$ in steps of $3°$. The z-dimension is divided into 129 points, separated by $12.5\,\text{mm}$. This means that at $8.0\,\text{GHz}$ the electric field is measured 3 times per wavelength, in the z-direction, and 1.5 times per wavelength, in the azimuth direction, respectively. Together, a total of $120 \times 129 = 15480$ measurement points are used for each radome configuration and frequency. The co- and cross-polarized measured electric fields are shown in Figure 1. The differences between the three different antenna and radome cases arise from constructive and destructive interference between the radiated field and the scattered field. In Figure 1 it is also observed that the electric field consists of a dominating co-component in the main lobe, *i.e.*, a dominating z-component since the antenna is vertically polarized.

3 The surface integral representation

The surface integral representation expresses the electromagnetic field in a homogeneous, isotropic region in terms of its values on the bounding surface. The representation states that if the electromagnetic field on a surface of a volume is known, the electromagnetic field in the volume can be determined [8, 16]. The representation is derived starting from the time harmonic Maxwell equations with the time conven-

tion $\mathrm{e}^{\mathrm{i}\omega t}$. The Maxwell equations transform into the vector Helmholtz equation

$$\nabla^2 \boldsymbol{E}(\boldsymbol{r}) + k^2 \boldsymbol{E}(\boldsymbol{r}) = 0 \tag{3.1}$$

since the material (air) is source free, homogeneous, and isotropic.

Assume that the electric field only consists of a component in the z-direction. This is a good approximation dealing with the specific measurements described in Section 2 since our prime interest is to reconstruct the electric field in the main lobe, where the z-component is clearly the dominating one, *cf.*, Figure 1.

Working with a scalar field, the surface integral representation only depends on the scalar electric field, E_z, and its normal derivative, $\partial E_z/\partial n$, *i.e.*, not all components of the electric and magnetic fields need to be included. Observe that in the vector integral representation all tangential components of the electric and magnetic fields must be taken into account [8]. The scalar surface integral representation is derived using the free space Green function $g(\boldsymbol{r}, \boldsymbol{r}') = \mathrm{e}^{-\mathrm{i}k|\boldsymbol{r}-\boldsymbol{r}'|}/4\pi|\boldsymbol{r} - \boldsymbol{r}'|$ giving [16]

$$\iint\limits_S \left[\frac{\partial g(\boldsymbol{r}, \boldsymbol{r}')}{\partial n} E_z(\boldsymbol{r}) - g(\boldsymbol{r}, \boldsymbol{r}') \frac{\partial E_z(\boldsymbol{r})}{\partial n} \right] \mathrm{d}S = \begin{cases} -E_z(\boldsymbol{r}') & \boldsymbol{r}' \in V \\ 0 & \boldsymbol{r}' \notin V \end{cases} \tag{3.2}$$

where V is the volume exterior to the closed surface S which consists of the radome surface with an added top and bottom surface. Observe that the electric field does not have to be zero outside the volume, *i.e.*, inside the radome. The surface integral representation (3.2) only states that the left-hand side of the equation, evaluated at a point $\boldsymbol{r}'$ outside the volume V, is zero, *i.e.*, the extinction theorem [16].

The equivalent surface currents are introduced as

$$M(\boldsymbol{r}) \equiv E_z(\boldsymbol{r}) \quad \text{and} \quad M'(\boldsymbol{r}) \equiv \frac{\partial E_z(\boldsymbol{r})}{\partial n} \tag{3.3}$$

which inserted in (3.2) give

$$\iint\limits_{\text{radome}} \left[\frac{\partial g(\boldsymbol{r}, \boldsymbol{r}')}{\partial n} M(\boldsymbol{r}) - g(\boldsymbol{r}, \boldsymbol{r}') M'(\boldsymbol{r}) \right] \mathrm{d}S = \begin{cases} -E_z^{\mathrm{cyl}}(\boldsymbol{r}') & \boldsymbol{r}' \in \text{cylinder} \\ 0 & \boldsymbol{r}' \in \text{surface inside radome} \end{cases} \tag{3.4}$$

where E_z^{cyl} is the z-component of the electric field on the measurement cylinder. The fictitious surface, inside the radome, is shaped as the radome and located close to the radome wall.

3.1 Angular Fourier transformation

Due to the measurement set-up, the transformation, the Green's function, is axially symmetric, see Section 2. The symmetry only applies to the transformation, not to the electric field. Thus, the left-hand side in (3.4) represents a convolution and by using a Fourier transformation of the azimuth coordinate, the computational complexity can be brought down one dimension. This reduction of one dimension, can be understood by writing the left-hand side in (3.4) as a matrix, X. This matrix

is a circulant matrix, *i.e.*, every row is shifted one step to the right compared to the previous row. The eigenvectors of all circulant matrices are the column vectors of the Fourier matrix, F. Multiplying a circulant matrix with the Fourier matrix, *i.e.*, performing the Fourier transformation, gives $FX = F\Lambda$ where Λ is a diagonal matrix, which can be seen as a reduction of one dimension [15].

The continuous variables in (3.4) are discretized to give linear matrix equations. The discretized cylindrical coordinate system is described by the integer indices depicted in Figure 3b. Discretization and Fourier transformation, in the azimuth coordinate, of (3.4) give

$$\sum_{m=0}^{N_m-1} \left[\widehat{\mathcal{G}}'_{im\hat{j}} \widehat{M}_{m\hat{j}} - \widehat{\mathcal{G}}_{im\hat{j}} \widehat{M}'_{m\hat{j}} \right] = -\widehat{E}^{\text{cyl}}_{i\hat{j}} \qquad \text{for all } i, \hat{j} \qquad (3.5)$$

and

$$\sum_{m=0}^{N_m-1} \left[\widehat{\mathsf{G}}'_{pm\hat{j}} \widehat{M}_{m\hat{j}} - \widehat{\mathsf{G}}_{pm\hat{j}} \widehat{M}'_{m\hat{j}} \right] = 0 \qquad \text{for all } p, \hat{j} \qquad (3.6)$$

where $\mathcal{G}$ and G are the surface integrals, taken over the radome, of the Green's function multiplied with the basis functions used in the discretization process. $\mathcal{G}$ has the discretized space variable $\boldsymbol{r}'$ belonging to the measurement cylinder and G has the discretized space variable $\boldsymbol{r}'$ belonging to the fictitious surface inside the radome, respectively. The prime denotes the normal derivative of the Green's function, $\hat{j}$ is the integer index belonging to the Fourier transformed azimuth component, and the "hat" denotes the Fourier transformed variables. The summation limits N_m and N_p are given in Figure 3b.

To solve the scalar surface integral representation, a limit process of (3.6) should be performed, letting the fictitious surface inside the radome approach the radome surface [2, 9]. To avoid singularities, we let the fictitious surface be located at a finite distance from the radome surface. This provides us with a simple and feasible method to allocate the surface currents, *i.e.*, the extinction theorem is used as an approximate solution to the integral representation in (3.6).

Reduction of M' in (3.5) and (3.6) gives

$$\sum_{m=0}^{N_m-1} \left\{ \widehat{\mathcal{G}}'_{im\hat{j}} - \sum_{p=0}^{N_p-1} \sum_{q=0}^{N_m-1} \widehat{\mathcal{G}}_{iq\hat{j}} (\widehat{\mathsf{G}}^{-1})_{qp\hat{j}} \widehat{\mathsf{G}}'_{pm\hat{j}} \right\} \widehat{M}_{m\hat{j}} = -\widehat{E}^{\text{cyl}}_{i\hat{j}} \quad \text{for all } i, \hat{j} \qquad (3.7)$$

Equation (3.7) can also be written as $\hat{j}$ matrix equations

$$\widehat{\boldsymbol{G}}^{\text{radome}}_{\hat{j}} \widehat{\boldsymbol{M}}_{\hat{j}} = -\widehat{\boldsymbol{E}}^{\text{cyl}}_{\hat{j}} \qquad \text{for all } \hat{j} \qquad (3.8)$$

where the matrices are defined as $\widehat{\boldsymbol{M}}_{\hat{j}} \equiv [\widehat{M}_{m1}]_{\hat{j}}$, $\widehat{\boldsymbol{E}}^{\text{cyl}}_{\hat{j}} \equiv [\widehat{E}^{\text{cyl}}_{i1}]_{\hat{j}}$, and

$$\widehat{\boldsymbol{G}}^{\text{radome}}_{\hat{j}} \equiv [\widehat{\mathcal{G}}'_{im}]_{\hat{j}} - [\widehat{\mathcal{G}}_{im}]_{\hat{j}} [\widehat{\mathsf{G}}_{mp}]^{-1}_{\hat{j}} [\widehat{\mathsf{G}}'_{pm}]_{\hat{j}} \qquad \text{for all } \hat{j} \qquad (3.9)$$

The used notation of matrices is that of [1].

3.2 Inversion with singular value decomposition

Since the matrices $\widehat{\boldsymbol{G}}_{\hat{\jmath}}^{\mathrm{radome}}$ and $[\widehat{\mathsf{G}}_{mp}]_{\hat{\jmath}}$ in (3.8) and (3.9) are not quadratic, a regular inversion cannot be performed. A fast and easy way to solve this is to use the singular value decomposition (SVD) [15]. This method is used on both matrices, but the SVD-equations are only given here for $\widehat{\boldsymbol{G}}_{\hat{\jmath}}^{\mathrm{radome}}$. The matrix system (3.8) can then be rewritten as

$$\widehat{\boldsymbol{U}}_{\hat{\jmath}}\widehat{\boldsymbol{S}}_{\hat{\jmath}}\widehat{\boldsymbol{V}}_{\hat{\jmath}}^{\dagger}\widehat{\boldsymbol{M}}_{\hat{\jmath}} = -\widehat{\boldsymbol{E}}_{\hat{\jmath}}^{\mathrm{cyl}} \qquad \text{for all } \hat{\jmath} \tag{3.10}$$

where $\widehat{\boldsymbol{V}}_{\hat{\jmath}}^{\dagger}$ denotes the Hermitian conjugate of $\widehat{\boldsymbol{V}}_{\hat{\jmath}}$. Both $\widehat{\boldsymbol{U}}_{\hat{\jmath}}$ and $\widehat{\boldsymbol{V}}_{\hat{\jmath}}$ are orthogonal matrices. $\widehat{\boldsymbol{S}}_{\hat{\jmath}}$ is a diagonal matrix consisting of the singular values to $\widehat{\boldsymbol{G}}_{\hat{\jmath}}^{\mathrm{radome}}$ in decreasing order. The singular values of both $\widehat{\boldsymbol{G}}_{\hat{\jmath}}^{\mathrm{radome}}$ and $[\widehat{\mathsf{G}}_{mp}]_{\hat{\jmath}}$ exhibit the tendency shown by the curves in Figure 4a.

A cut-off value, δ, normalized to the operator L_2-norm of $\widehat{\boldsymbol{G}}_{1}^{\mathrm{radome}}$ is chosen. The operator L_2-norm of $\widehat{\boldsymbol{G}}_{1}^{\mathrm{radome}}$ is equal to the largest singular value (σ_1) of the largest Fourier transformed azimuth component [9]. All singular values smaller than δ are ignored during the inversion of $\widehat{\boldsymbol{S}}_{\hat{\jmath}}$ and are afterwards set to zero. If this is not done the small singular values create an uncontrolled growth of non-radiation currents when inverted. The mathematical formulation then fails since very small electric field contributions become dominating. Performing the inversion of (3.10) gives

$$\widehat{\boldsymbol{M}}_{\hat{\jmath}} = -\widehat{\boldsymbol{V}}_{\hat{\jmath}}\widehat{\boldsymbol{S}}_{\hat{\jmath}}^{-1}\widehat{\boldsymbol{U}}_{\hat{\jmath}}^{\dagger}\widehat{\boldsymbol{E}}_{\hat{\jmath}}^{\mathrm{cyl}} \qquad \text{for all } \hat{\jmath} \tag{3.11}$$

Before the system of equations is solved, it is necessary to convert it back from Fourier space by an inverse Fourier transformation

$$\boldsymbol{M}_{j} = \mathcal{F}^{-1}\left[-\widehat{\boldsymbol{V}}_{\hat{\jmath}}\widehat{\boldsymbol{S}}_{\hat{\jmath}}^{-1}\widehat{\boldsymbol{U}}_{\hat{\jmath}}^{\dagger}\widehat{\boldsymbol{E}}_{\hat{\jmath}}^{\mathrm{cyl}}\right] \qquad \text{for all } j,\hat{\jmath} \tag{3.12}$$

where j, as above, denotes the integer index belonging to the discretized azimuth component, see Figure 3b.

4 Implementation

Some adjustments of the formulas are made in the implementation process. To facilitate the calculations, the radome surface is reshaped into a closed surface by adding a smooth top and bottom surface. These extra surfaces are useful since the measurements are performed under non-ideal conditions. The turntable, on which the antenna and radome are located, see Figure 2, reflects some of the radiation, which is taken care of by the added bottom surface. The top surface takes care of the electric field that is reflected on the inside of the radome and then radiated through
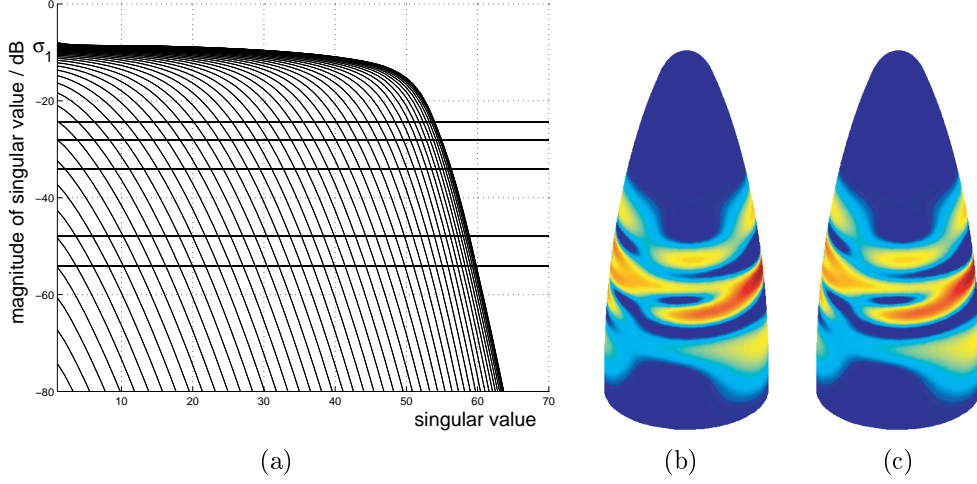
(a)   (b)   (c)

Figure 4: (a) The typical behavior of singular values of $\widehat{\boldsymbol{G}}_{\hat{\jmath}}^{\mathrm{radome}}$ and $[\widehat{\mathsf{G}}_{mp}]_{\hat{\jmath}}$. Every curve represents the singular values of a Fourier transformed azimuth component, *i.e.*, different $\hat{\jmath}$. The horizontal lines describe the cut-off values, $\delta = \sigma_1[0.15\ 0.1\ 0.05\ 0.01\ 0.005]$. (b) The synthetic equivalent currents, originating from three dipoles, in a dB-scale $[-15, 0]$, normalized to the highest current value, *i.e.*, the maximum current magnitude in subfigure c. (c) The reconstructed currents in dB-scale $[-15, 0]$, normalized to its highest current value.

the top hole. If these factors are not considered, unwanted edge effects occur since the electric field originating from the turntable and the top of the radome is forced to arise from the radome itself.

The measured electric near field is only measured 1.5 times per wavelength, in the azimuth direction, at the frequency 8.0 GHz, see Section 2. To be sure that the equivalent currents on the radome are recreated in an accurate way, it is necessary to have a high sample density on the radome. This is achieved by increasing the number of discrete points, in the azimuth direction, on the radome surface by including extra angles between the already existing ones. Thus, the axial symmetry of the Green's transformation is preserved.

The sample density on the measurement cylinder contributes very little to the total error. The scalar surface integral representation creates currents on the radome such that the electric field is correct at the measurement points. However, if the Nyquist theorem is fulfilled, then the electric field is correct at all points on the measurement surface, *i.e.*, not only at the measurement points [15]. As mentioned above, the amount of data is large and the matrix $\widehat{\boldsymbol{G}}^{\mathrm{radome}}$, *cf.*, (3.9), has approximately 10^8 elements at the frequency 8.0 GHz when the sample density is 10 points per wavelength both in the azimuth direction and in the z-direction on the radome.

To verify and find the error of the method, synthetic data is used. A synthetic electric field, originating from three dipoles inside the radome is shown in Figure 4b. The corresponding reconstructed currents on a surface shaped as the radome are shown in Figure 4c where the sample density is 10 points per wavelength both in
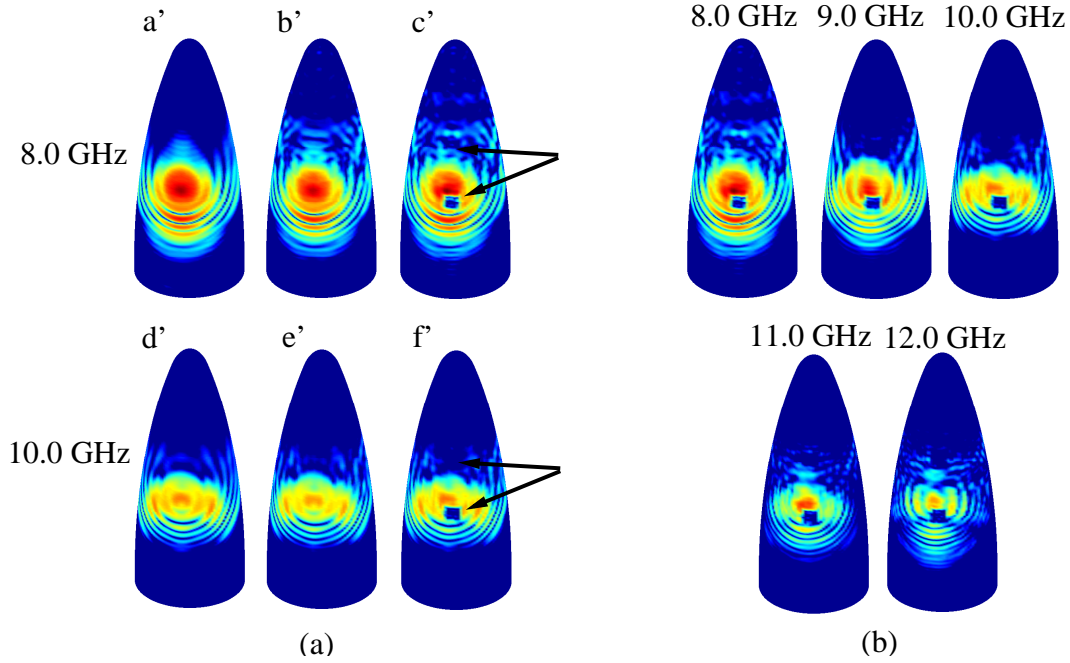
Figure 5: The reconstructed currents in dB-scale $[-30, 0]$, all normalized to the highest current value, *i.e.*, the maximum current magnitude in figure ac'. (a) The different measurement configurations are depicted at two different frequencies. From left to right; antenna without radome, antenna together with radome, and antenna together with defect radome, respectively. The arrows point out the location of the copper plates on the defect radome. (b) The defect radome case, shown at different frequencies.

the z-direction and in the azimuth direction. The inner fictitious surface is located one wavelength from the radome surface.

The error as a function of the Fourier transformed azimuth angle component is defined as

$$
\begin{aligned}
\mathrm{Err}(\hat{\jmath}) &= 20 \log_{10} \frac{\| \; \widehat{\boldsymbol{M}}_{\hat{\jmath}} - \widehat{\boldsymbol{M}}_{\hat{\jmath}}^{\mathrm{correct}} \; \|_2}{\| \; \widehat{\boldsymbol{M}}_{\hat{\jmath}}^{\mathrm{correct}} \; \|_2} \\
&= 20 \log_{10} \frac{\sqrt{\sum_{m=0}^{N_m-1} | \; \widehat{M}_{m\hat{\jmath}} - \widehat{M}_{m\hat{\jmath}}^{\mathrm{correct}} \; |^2 \, \Delta S_m}}{\sqrt{\sum_{m=0}^{N_m-1} | \; \widehat{M}_{m\hat{\jmath}}^{\mathrm{correct}} \; |^2 \, \Delta S_m}} \quad \text{for all } \hat{\jmath}
\end{aligned}
\tag{4.1}
$$

where ΔS_m denotes the discretized area elements on the radome.

By using synthetic data and choosing appropriate cut-off values, δ, the error is shown to be below $-60\,\mathrm{dB}$ for each existing Fourier transformed azimuth angle component. To obtain these low error levels, the measurement surface must be closed, *i.e.*, field values at the top and bottom surfaces of the cylindrical measurement surface must be included. The cut-off values depend on the complexity of the specific measurement set-up and must be investigated for each new set-up.
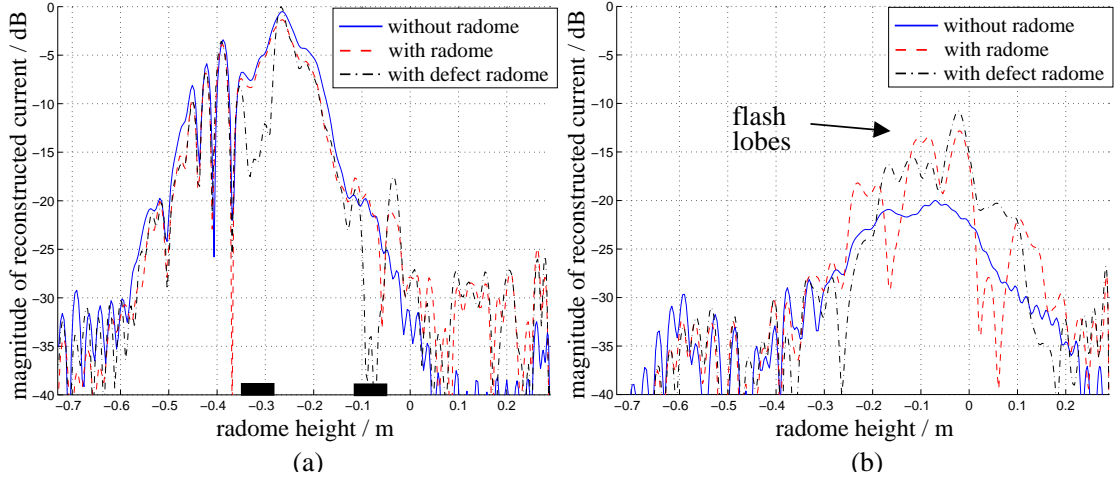
Figure 6: Cross section of the reconstructed currents, on the radome surface, for the different measurement configurations at 8.0 GHz. The currents are shown as functions of the radome height for a fixed angle. All graphs are normalized to the highest current value, *i.e.*, the maximum current for the defect radome case. (a) The graph representing the currents in the main lobe, *i.e.*, the front of the radome. The positions of the copper plates are marked by thick lines on the horizontal axis. (b) The currents on the back of the radome.

The total error of the scalar surface integral representation using the measured near field described in Section 2 is hard to define since the noise level and the amount of field spread outside the measurement cylinder are unknown parameters. Instead, we rely on the fact that the method handles synthetic data well and that the results using measured data is satisfactory, see Section 5.

5 Results using measured near-field data

The measured near-field data, described in Section 2, is investigated. The inner fictitious surface is located one wavelength from the radome surface. The sample density on the radome is 10 points per wavelength both in the azimuth direction and in the z-direction. The cut-off values are determined in accordance with the discussion in Section 4.

Three different measurement configurations are investigated, *viz.*, antenna, antenna together with radome, and antenna together with defect radome. The studied frequency interval is $8.0 - 12.0$ GHz. The results for the different measurement configurations are shown in Figure 5a at the frequencies 8.0 GHz and 10.0 GHz. In Figure 5b the results for the defect radome case are shown for the frequencies 8.0 GHz, 9.0 GHz, 10.0 GHz, 11.0 GHz, and 12.0 GHz, respectively.

In the case when no radome is located around the antenna, the equivalent currents are calculated on a surface shaped as the radome, see Figure 5aa' and 5ad'.
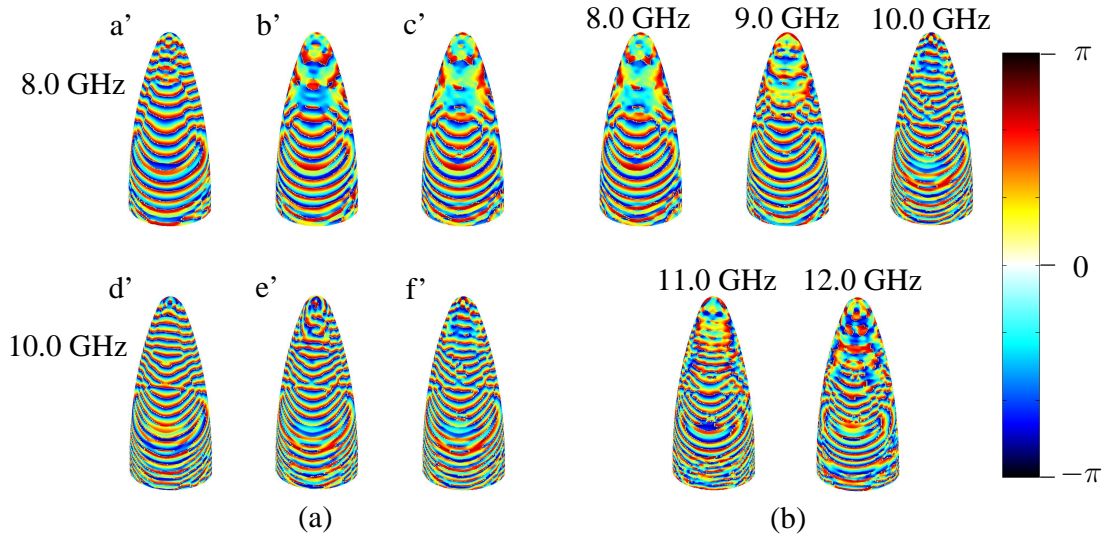
Figure 7: The reconstructed phase of the currents on the front of the radome. (a) The different measurement configurations are depicted at two different frequencies. From left to right; antenna without radome, antenna together with radome, and antenna together with defect radome, respectively. (b) The defect radome case, shown at different frequencies.

The figures show that the near field close to the antenna is complex and hard to predict, *i.e.*, the diffraction pattern must be taken into account. The diffraction is explained as environmental reflections and an off-centered antenna feed.

The case when the radome is present, see Figure 5ab' and 5ae', shows in comparison to the case without radome that the radome interacts with the antenna and hence disturbs the radiated field. However, the currents in the main lobe are hardly affected by the radome, as seen in Figure 6a. The influence of the radome is clearly visible in the reconstructed currents on the back of the radome where flash lobes occur, see Figure 6b.

The defect radome has two copper plates attached to its surface. These are located in the forward direction of the main lobe of the antenna and centered at the heights 41.5 cm and 65.5 cm above the bottom of the radome. The length of the side of the squared copper plates is 6 cm, which corresponds to 1.6 wavelengths at 8.0 GHz and 2.4 wavelengths at 12.0 GHz, respectively. The locations of the copper plates are detected as shown in Figure 5ac' and 5af', where the lower plate appears clearly. The other plate is harder to discern since it is located in a region with low amplitudes. However, a cross section graph through the main lobe detects even this copper plate, see Figure 6a. Observe that the effects of the copper plates cannot be localized directly in the near-field data, compare Figure 6a to Figure 1a. The near-field data only shows that the field is disturbed, not the location of the disturbance. Nevertheless, by using the scalar surface integral representation, the effects of the plates are localized and focused. The defect radome also increases the backscattering
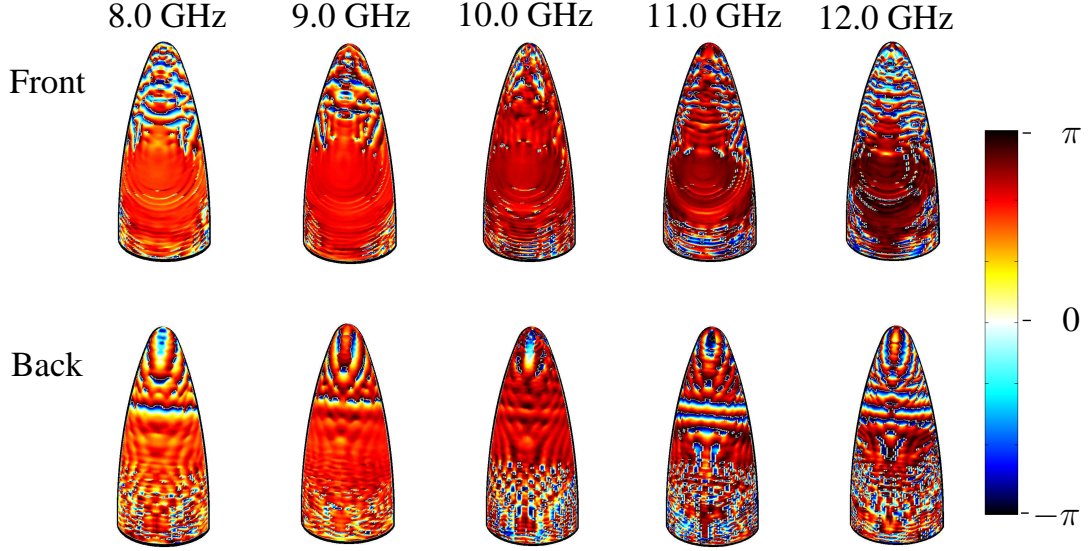
8.0 GHz   9.0 GHz   10.0 GHz   11.0 GHz   12.0 GHz

Front

Back

Figure 8: The phase difference (antenna - antenna with radome) for several frequencies.

as seen in Figure 6b. Due to the copper plates, the flash lobes are different compared to the case with the non-defect radome.

Until now only the amplitude of the reconstructed currents has been investigated. The phase of the currents is depicted in Figure 7. The vertical lines above the main lobe in Figure 7a' and 7d' are due to phase jumps and are caused by the low amplitude of the currents in these areas. The phase difference (antenna - antenna with radome) reveals how the the phase is changed due to the influence of the radome, see Figure 8. The phase shift, denoted Δ_φ, is only known modulus 2π. The phase shift in the main lobe is almost constant, especially for the low frequencies, which is more clearly seen by looking at the cross section of the front side of the radome, see Figure 9. What is noticeable in this image is the region between $z = -0.4$ m and $z = 0$ m, *i.e.*, the main lobe where the phase shift is nearly constant. In areas where the amplitude of the field is small, *cf.*, Figure 6a, the phase of the field is not well defined, *i.e.*, it is dominated by noise. This almost constant phase shift, for the low frequencies, confirms that the radome is quite well adapted to the frequencies $8.0 - 9.0$ GHz, which is also the frequency interval where the antenna is well matched, see Section 2.

Sometimes, when dealing with phase information, the figures can be clarified by using phase unwrapping [4]. It means that the jump in the scale between 0 and 2π is removed. In our case phase unwrapping gives us no new information since the area of interest is the main lobe and the phase shift there is almost constant.

To validate the calculation of the phase shift, the propagation distance of the field through the radome, *i.e.*, the actual propagation path of the field in the radome
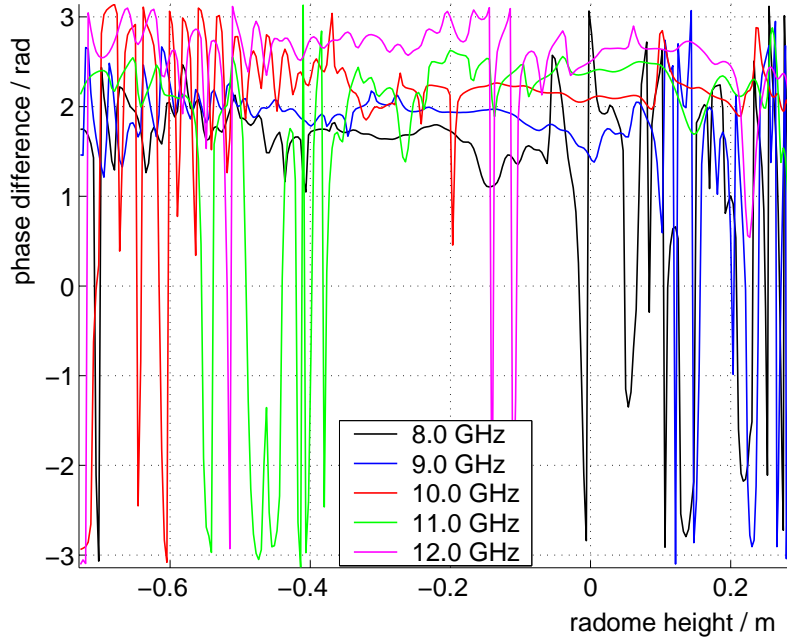
Figure 9: Cross section of the phase difference (antenna - antenna with radome) on the front of the radome. Observe that in areas where the amplitude of the currents are small, *cf.*, Figure 6a, the phase of the field is not well defined, *i.e.*, it is dominated by noise.

material, is estimated and compared to the actual thickness of the radome given in Section 2. The propagation distance of the field through the radome is longer than the wall thickness since the field has an incident angle larger than zero. The phase difference between two fields propagating the distance d in air and in the radome material, respectively, can be written as [12]

$$\Delta_\varphi = \text{Re}\left[2\pi f \sqrt{\epsilon_0 \epsilon_r \mu_0 (1 - \mathrm{i}\tan\delta)}\right] d - 2\pi f \sqrt{\epsilon_0 \mu_0}\, d \qquad (5.1)$$

where f is the frequency, d the propagation distance of the field, ϵ_0 the permittivity of vacuum, and μ_0 the permeability of vacuum, respectively. The parameters belonging to the radome, described in Section 2, are the relative permittivity, ϵ_r, and the loss tangent, $\tan\delta$. Since only an estimation of the propagation distance is performed, we assume that this distance is the same in both air and the radome material. We assume perpendicular incidence and neglect all reflections. According to Section 2, the thickness of the radome is between $7.6 - 8.2\,\text{mm}$. The almost constant phase shifts in the main lobe are approximated from Figure 9 for all frequencies. Solving for d in (5.1) results in a propagation distance of $9.3 - 9.7\,\text{mm}$ for all frequencies, which is considered constant due to the crude approximations of the phase shifts. The phase shift, Δ_φ, is comparable to the insertion phase delay (IPD) often used in the radome industry.

The phase images in Figure 7b are not appropriate for finding the location of the copper plates. Instead, the phase difference (antenna with radome - antenna with
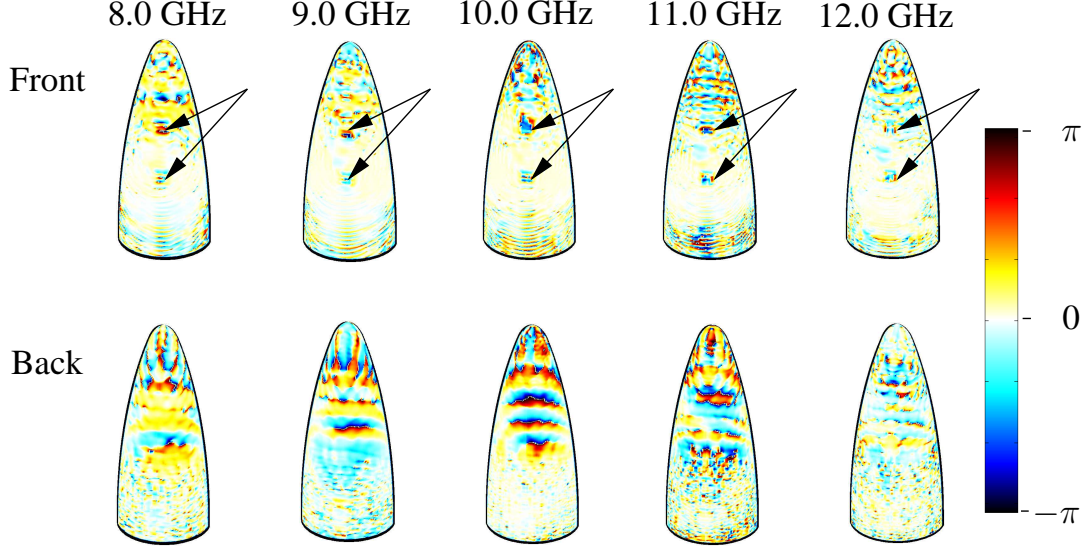
Figure 10: The phase difference (antenna with radome - antenna with defect radome) for several frequencies. The arrows point out the location of the copper plates.

defect radome) is useful, see Figure 10. These images reveal the change of the phase due to the attached copper plates on the defect radome.

As a final verification of the method, the amplitude on a sphere in the far-field region is studied. The electric field, originating from the equivalent currents on the radome, is calculated on the sphere, *i.e.*,

$$\boldsymbol{E}_j^{\mathrm{sph}} = -\mathcal{F}^{-1}\left[\widehat{\boldsymbol{G}}_{\hat{\jmath}}\widehat{\boldsymbol{M}}_{\hat{\jmath}}\right] \qquad \text{for all } j, \hat{\jmath} \tag{5.2}$$

in accordance with (3.8) and (3.12), except that $\widehat{\boldsymbol{G}}_{\hat{\jmath}}$ now describes the transformation from the radome to the inner fictitious surface and to the far-field sphere. The denotions j and $\hat{\jmath}$ are, as above, the integer index belonging to the discretized azimuth component and the Fourier transformed discretized azimuth component, respectively.

The far-field amplitude F is derived as

$$F(\theta, \phi) = kr\, \mathrm{e}^{\mathrm{i}kr} E^{\mathrm{sph}}(r, \theta, \phi) \qquad \text{as } r \to \infty \tag{5.3}$$

where (r, θ, ϕ) denotes the spherical coordinate system [7]. The result is compared with far-field data, supplied by Applied Composites AB, as shown in Figure 11. The far field is depicted for the angles $\phi = 0$ and $\phi = \pi$, *i.e.*, a cross-section through the far field of the main lobe and the corresponding far field originating from the currents on the back of the radome. There is a lack of agreement between the measured far field and the calculated one at the angles corresponding to the top of the radome, *i.e.*, $\theta \approx 0$. This is due to the fact that fields originating hereof are
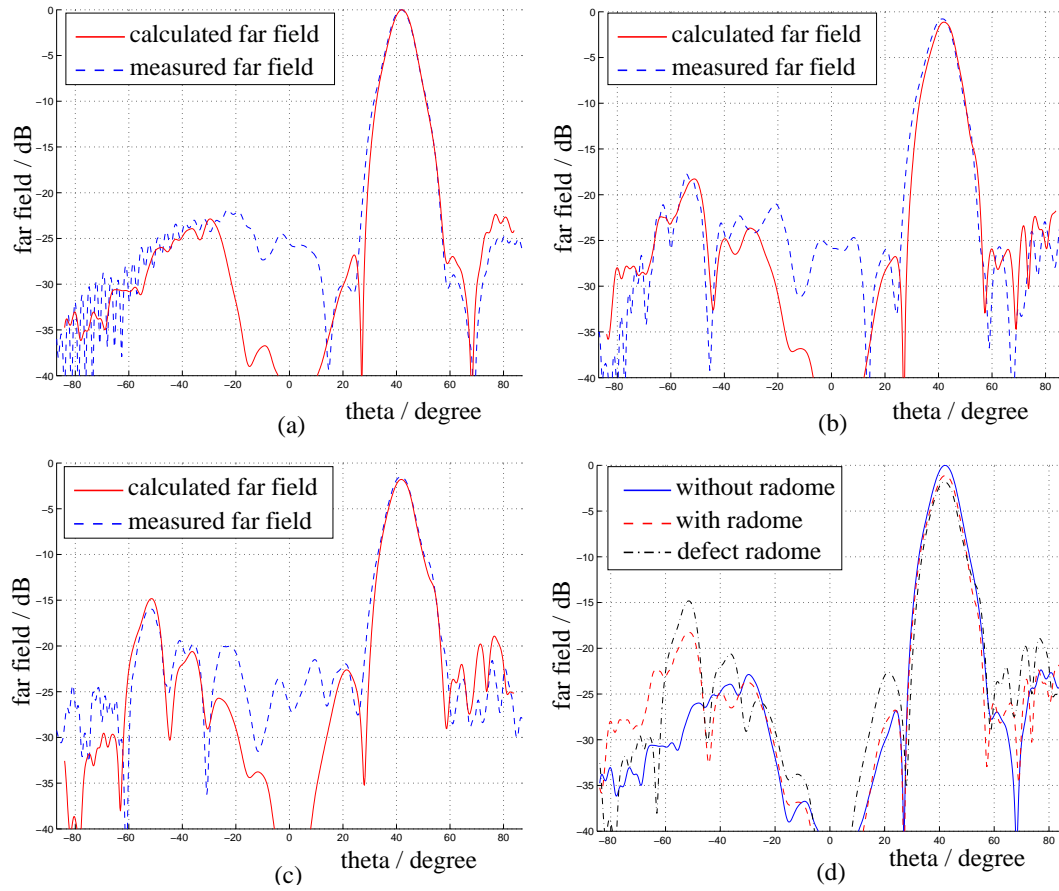
Figure 11: Comparison between the measured far-field data, supplied by Applied Composites AB, and the far field calculated from the equivalent currents on the radome surface. The far fields are normalized to the maximum value of the far field when no radome is present. (a) Antenna without radome. (b) Antenna together with radome. (c) Antenna together with defect radome. (d) The calculated far-field pattern for the three measurement configurations.

not all included in the measured near-field data, since the measurement surface is a cylinder, see Figure 3a. The fact that the radome disturbs and reflects the electric field, as earlier seen in Figure 6b, can also be detected in the far field, see Figure 11d, where flash lobes appear when the radome is present.
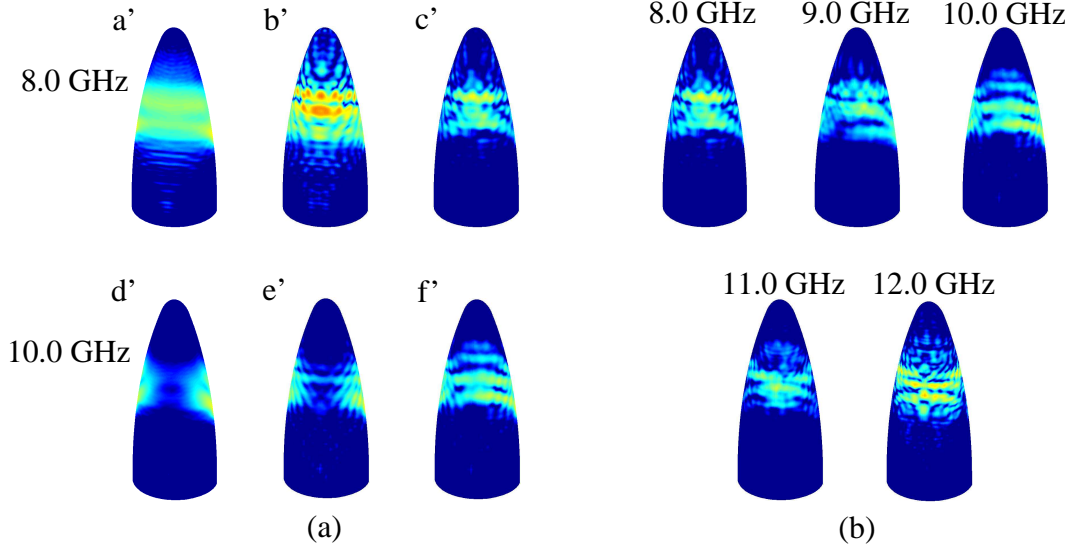
Figure 12: The reconstructed currents on the back of the radome in a dB-scale $[-30, 0]$, all normalized to the highest current value, *i.e.*, the maximum current magnitude in Figure 5ac'. (a) The different measurement configurations are depicted at two different frequencies. From left to right; antenna without radome, antenna together with radome, and antenna together with defect radome, respectively. (b) The defect radome case, shown at different frequencies.

6 Alternative ways to visualize the electromagnetic currents

6.1 Amplitude of the reconstructed currents

In the previous section, the amplitude and the phase of the reconstructed currents have been visualized by showing the amplitude in dB-scale over the front side of the radome in Figure 5, and over a cross section of the front and the back in Figure 6. These ways of presenting the results are in this section supplemented in an attempt to see what possibilities other visualization approaches offer. First, the back side of the radome is shown in a dB-scale in Figure 12. The absolute value of the currents is also displayed in a linear scale on the front and the back of the radome in Figures 13 and 14, respectively. The flash lobes clearly appear in both dB- and linear scale, see Figures 12 and 14. Notice that the top copper plate is not resolved very well in the linear scale compared to the dB-scale in Figure 5.
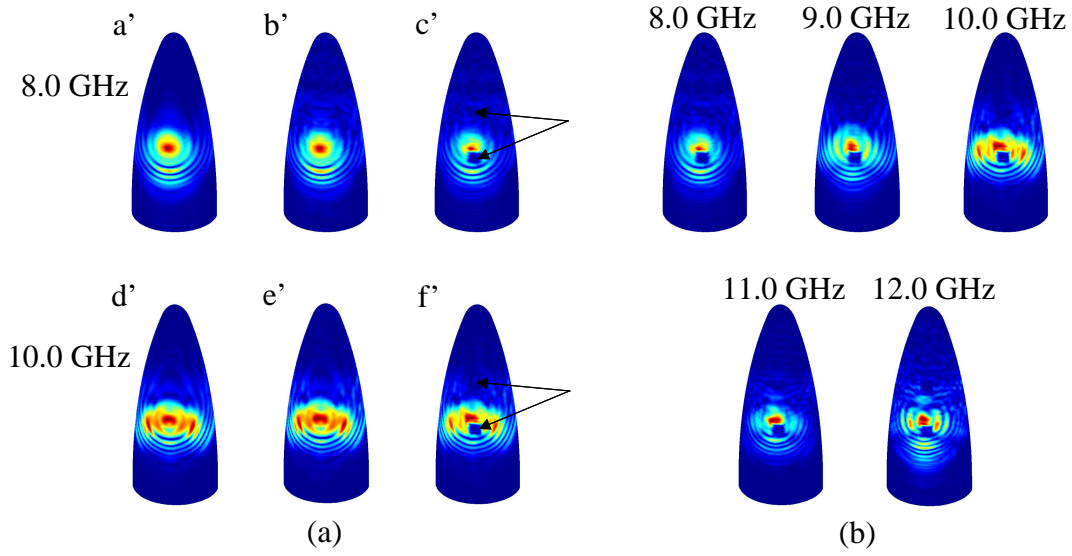
Figure 13: The reconstructed currents on the front of the radome in a linear scale, all normalized to the highest current value, *i.e.*, the maximum current magnitude in figure ac'. (a) The different measurement configurations are depicted at two different frequencies. From left to right; antenna without radome, antenna together with radome, and antenna together with defect radome, respectively. The arrows point out the location of the copper plates on the defect radome. (b) The defect radome case, shown at different frequencies.

6.2 Differences between the measurement configurations

To further demonstrate the distinctions between the three radome configurations their differences are calculated. The difference (|antenna| - |antenna with radome|) is shown in Figure 15 in a dB-scale, and in Figure 16 in a linear scale. The images show the influence of the radome and the appearance of flash lobes at the back of the radome. The dB-scale, Figure 15, has the advantage that also small current values are made visible. The advantage with the linear scale is that the sign of the difference is visible. In Figure 16, on the front of the radome, the field originating from the antenna is the strongest, *i.e.*, the difference is positive, while on the back of the radome, the field passing trough the radome as flash lobes is the strongest, *i.e.*, the difference is negative. This conclusion can not be drawn by looking at the dB-scale in Figure 15, where only the amplitude of the difference is displayed.

To emphasize the contribution of the defect radome, the difference (|antenna with radome| - |antenna with defect radome|) is studied in a dB-scale, see Figure 17 and in a linear scale, see Figure 18. The effect of the lower copper plate is clearly detectable in both figures, while the top plate is hard to discern in both scales, *i.e.*, these figures are useful to get an overview, but when it comes to details, other visualizations approaches are needed. The tricky part with the dB-scale is to choose its lower limit. If a too low value is used, too much noise appears and blurs the
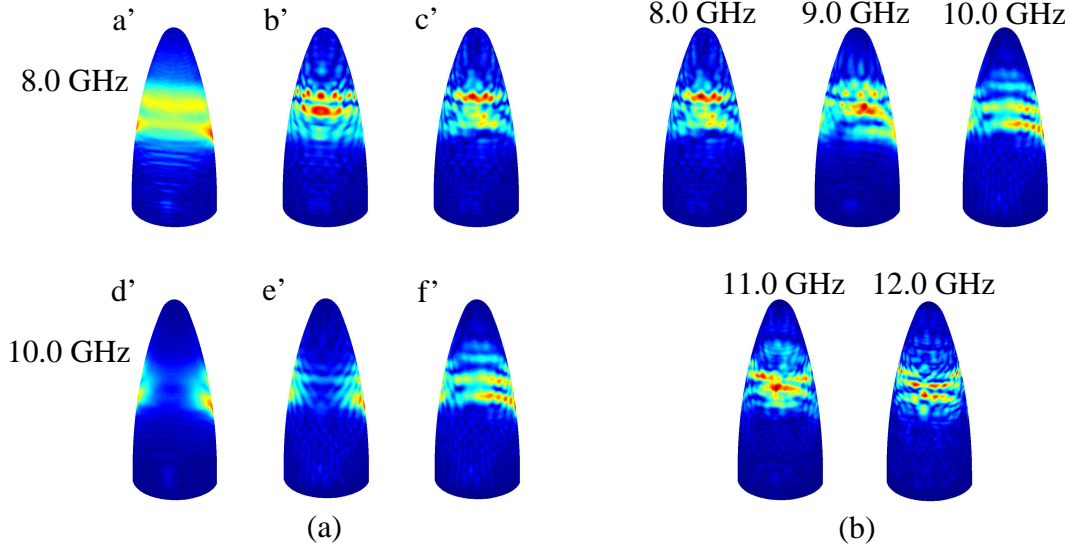
Figure 14: The reconstructed currents on the back of the radome in a linear scale, all normalized to the highest current value, *i.e.*, the maximum current magnitude in Figure 13ac'. (a) The different measurement configurations are depicted at two different frequencies. From left to right; antenna without radome, antenna together with radome, and antenna together with defect radome, respectively. (b) The defect radome case, shown at different frequencies.

image. However, if instead a too high value is picked, the field effects caused by the copper plates are hidden. To reveal the exact positions of the copper plates, cross section graphs through the front of the radome are presented in a linear and in a dB-scale in Figure 19 for the frequency 8.0 GHz. The effects of the copper plates are clearly seen in both scales, but their positions are somewhat off-centered. This is probably due to the fact that the copper plates cause diffractions and reflections, which do not occur when only the radome is present. There is also an uncertainty in the measurement set-up.

6.3 Propagation of the reconstructed fields

To see how the waves propagate on the radome-shaped surface, the field values, *i.e.*, $\mathrm{Re}\,(\boldsymbol{M}\,\mathrm{e}^{\mathrm{i}\omega t})$ for $0 \leq \omega t \leq 2\pi$, are presented as a movie on `http://www.eit.lth.se/staff/kristin.persson` under the link `Research`. The distinctions between the different frequencies and radome configurations are revealed on both the front and the back side of the radome surface.

7 Discussion and conclusions

The scalar surface integral representation gives a linear map between the equivalent currents and the near-field data for general geometries. It is shown that this map
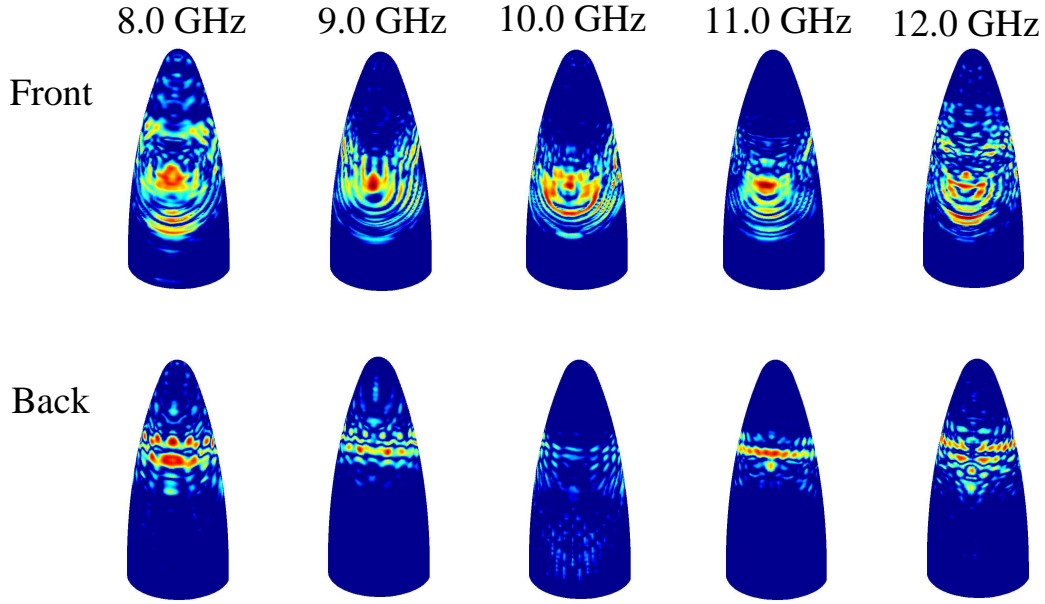
8.0 GHz   9.0 GHz   10.0 GHz   11.0 GHz   12.0 GHz

Front

Back

Figure 15: The amplitude difference abs(|antenna| - |antenna with radome|) for several frequencies. The amplitude differences are normalized to the highest value at each frequency and are all depicted in a dB-scale $[-20, 0]$.

can be inverted for axially symmetric geometries. The model can theoretically be adapted to geometries lacking symmetry axes. Although it is not a feasible approach for radome applications, demanding large quantities of measured data, with the present computer capacity.

The transformation method is stable and useful in radome design and for evaluation purposes. To investigate the electric field passing through the radome, the current distribution on the antenna or on a surface enclosing the antenna must be known. Using the surface integral representation, the equivalent currents, on a surface enclosing the antenna, can be described. The insertion phase delay is estimated by investigating the phase of the reconstructed currents.

In this paper, copper plates are attached on the radome, in the direction of the antenna main lobe. The length of the side of the square copper plates is $1.6 - 2.4$ wavelengths, corresponding to the frequency span $8.0 - 12.0$ GHz. The effects of the plates cannot be localized directly by using the near-field data, but by using the equivalent currents, the effects are focused and detected on the radome surface. Thus, by transforming the near-field data to the radome surface, field defects introduced by the radome and other disturbances are focused back to their origins. Another range of application within the radome industry is to study how *e.g.*, lightning conductors and Pitot tubes, often placed on radomes, influence the equivalent currents. We predict that such influences and the field effects of the radome itself can be detected.

It is concluded that the transformation method based on the scalar surface integral representation works very well and that the field of applications is large. A
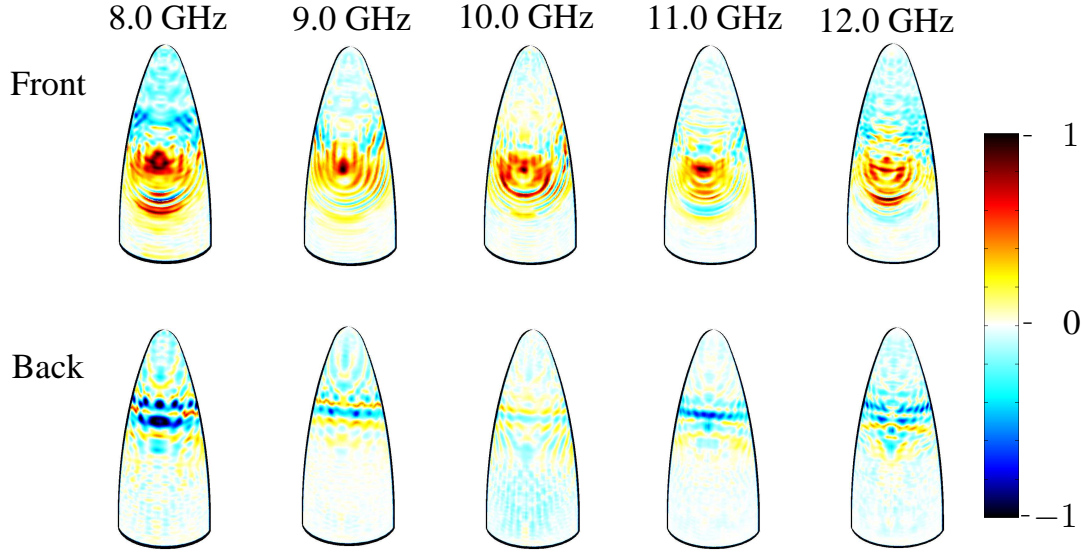
22

Figure 16: The amplitude difference (|antenna| - |antenna with radome|) for several frequencies. The amplitude differences are normalized to the highest value at each frequency and are all depicted in a linear scale.

natural continuation is to elaborate the algorithm by including near-field data with cross-polarization, *i.e.*, to implement the full Maxwell equations with a Method of Moments (MoM). Nevertheless, if the measured near-field data consists of one dominating component, the use of the full Maxwell equations are not necessary, as shown in this paper.

Additional aspects to be investigated more thoroughly in the future are the resolution possibilities of manufacturing errors and other external field influences. Moreover, a study regarding the detection of different materials attached to the radome surface is desirable.

Acknowledgments

References

[1] H. Anton. *Elementary Linear Algebra*. John Wiley & Sons, New York, 7 edition, 1994.

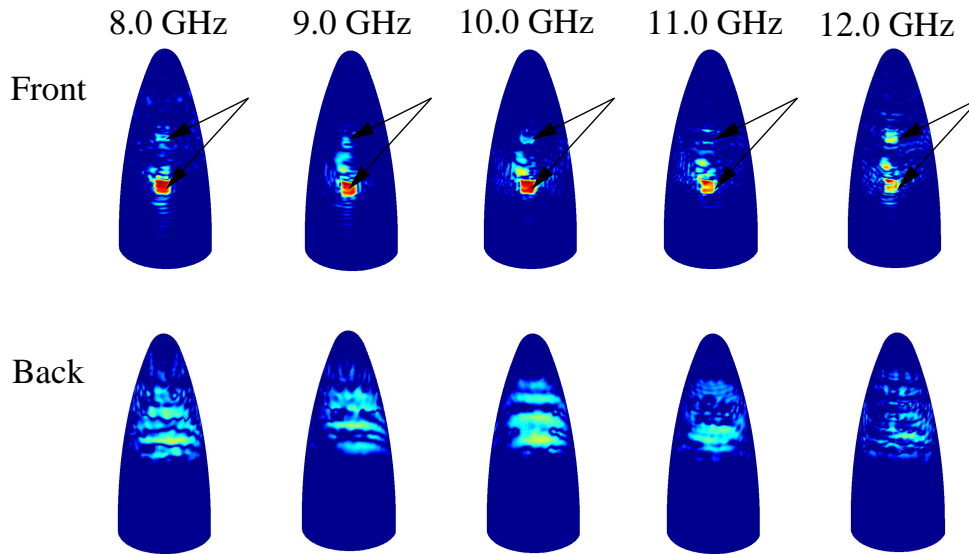**Figure 17**: The amplitude difference abs(|antenna with radome| - |antenna with defect radome|) for several frequencies. The amplitude differences are normalized to the highest value at each frequency and are all depicted in a dB-scale $[-30, 0]$. The arrows point out the location of the copper plates.

[2] C. A. Balanis. *Antenna Theory*. John Wiley & Sons, New York, second edition, 1997.

[3] L. E. Corey and E. B. Joy. On computation of electromagnetic fields on planar surfaces from fields specified on nearby surfaces. *IEEE Trans. Antennas Propagat.*, **29**(2), 402–404, 1981.

[4] D. C. Ghiglia and M. d. Pritt. *Two-Dimensional Phase Unwrapping: theory, algorithms, and software*. John Wiley & Sons, New York, 1998.

[5] J. Hanfling, G. Borgiotti, and L. Kaplan. The backward transform of the near field for reconstruction of aperture fields. *IEEE Antennas and Propagation Society International Symposium*, **17**, 764–767, 1979.

[6] J. E. Hansen, editor. *Spherical Near-Field Antenna Measurements*. Number 26 in IEE electromagnetic waves series. Peter Peregrinus Ltd., Stevenage, UK, 1988. ISBN: 0-86341-110-X.

[7] J. D. Jackson. *Classical Electrodynamics*. John Wiley & Sons, New York, second edition, 1975.

[8] D. S. Jones. *Acoustic and Electromagnetic Waves*. Oxford University Press, New York, 1986.

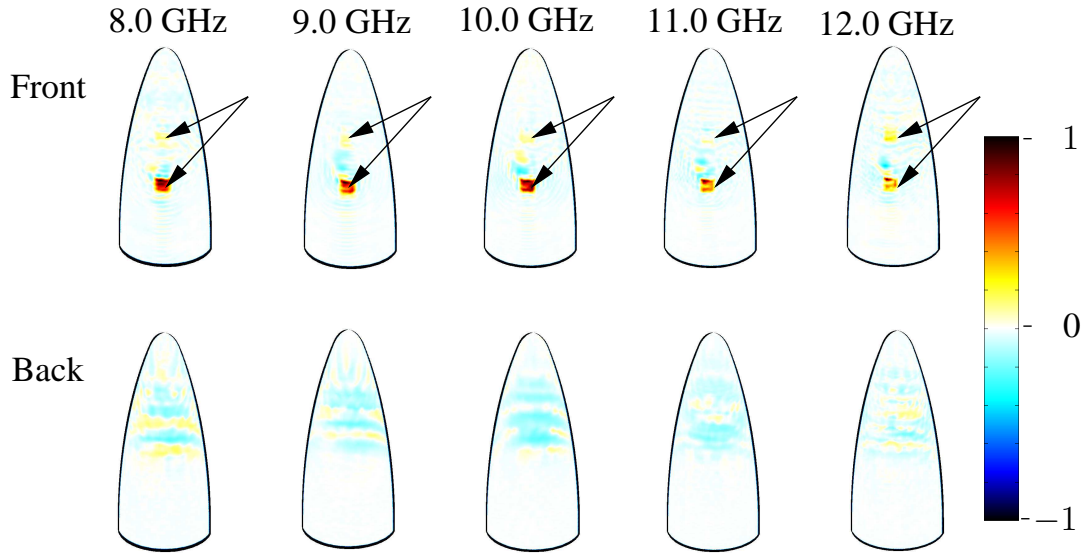[9] R. Kress. *Linear Integral Equations*. Springer-Verlag, Berlin Heidelberg, second edition, 1999.

24

Figure 18: The amplitude difference (|antenna with radome| - |antenna with defect radome|) for several frequencies. The amplitude differences are normalized to the highest value at each frequency and are all depicted in a linear scale. The arrows point out the location of the copper plates.

[10] J. Lee, E. M. Ferren, D. P. Woollen, and K. M. Lee. Near-field probe used as a diagnostic tool to locate defective elements in an array antenna. *IEEE Trans. Antennas Propagat.*, **36**(6), 884–889, 1988.

[11] K. Persson and M. Gustafsson. Reconstruction of equivalent currents using a near-field data transformation – with radome applications. *Progress in Electromagnetics Research*, **54**, 179–198, 2005.

[12] D. M. Pozar. *Microwave Engineering*. John Wiley & Sons, New York, 1998.

[13] Y. Rahmat-Samii, L. I. Williams, and R. G. Yaccarino. The UCLA bi-polar planar-near-field antenna-measurement and diagnostics range. *IEEE Antennas and Propagation Magazine*, **37**(6), 16–35, December 1995.

[14] T. K. Sarkar and A. Taaghol. Near-field to near/far-field transformation for arbitrary near-field geometry utilizing an equivalent electric current and MoM. *IEEE Trans. Antennas Propagat.*, **47**(3), 566–573, March 1999.

[15] G. Strang. *Introduction to applied mathematics*. Wellesley-Cambridge Press, Box 157, Wellesley MA 02181, 1986.

[16] S. Ström. Introduction to integral representations and integral equations for time-harmonic acoustic, electromagnetic and elastodynamic wave fields. In V. V. Varadan, A. Lakhtakia, and V. K. Varadan, editors, *Field Representations*
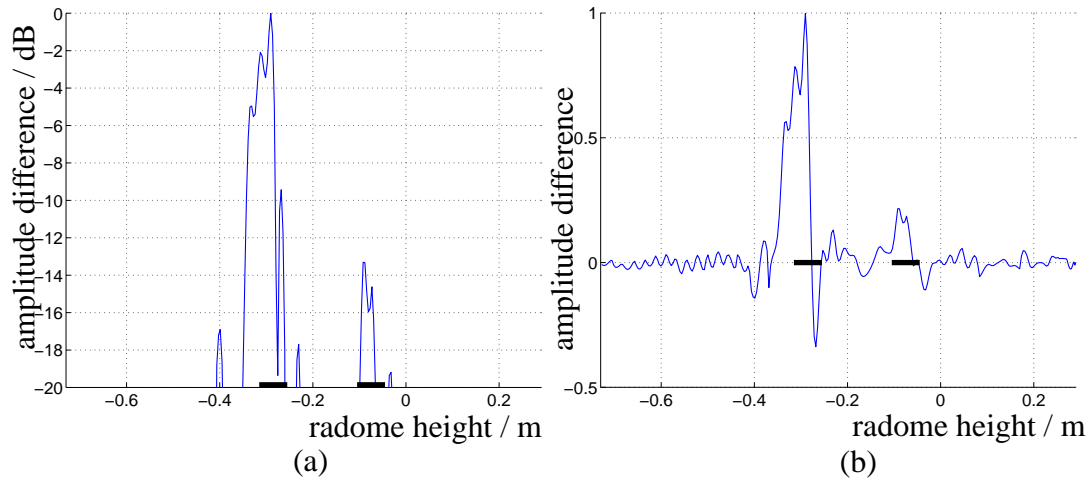
Figure 19: Cross section of the amplitude difference (|antenna with radome| - |antenna with defect radome|) at 8.0 GHz. The graphs show the difference on the front of the radome as a function of the radome height for a fixed angle. They are both normalized to their highest values. The positions of the copper plates are marked by thick lines on the horizontal axis. (a) The difference abs(|antenna with radome| - |antenna with defect radome|) in dB-scale. (b) The difference (|antenna with radome| - |antenna with defect radome|) in a linear scale.

and *Introduction to Scattering*, volume 1 of *Handbook on Acoustic, Electromagnetic and Elastic Wave Scattering*, chapter 2, pages 37–141. Elsevier Science Publishers, Amsterdam, 1991.

[17] V. V. Varadan, Y. Ma, V. K. Varadan, and A. Lakhtakia. Scattering of waves by spheres and cylinders. In V. V. Varadan, A. Lakhtakia, and V. K. Varadan, editors, *Field Representations and Introduction to Scattering*, volume 1 of *Handbook on Acoustic, Electromagnetic and Elastic Wave Scattering*, chapter 4, pages 211–324. Elsevier Science Publishers, Amsterdam, 1991.

[18] M. B. Woodworth and A. D. Yaghjian. Derivation, application and conjugate gradient solution of dual-surface integral equations for three-dimensional, multi-wavelength perfect conductors. *Progress in Electromagnetics Research*, **5**, 103–129, 1991.

[19] A. D. Yaghjian. An overview of near-field antenna measurements. *IEEE Trans. Antennas Propagat.*, **34**(1), 30–45, January 1986.